NANOSTRUCTURED MATERIALS—PROCESSING, STRUCTURES, PROPERTIES, APPLICATIONS

Plasticity initiation and subsequent deformation behavior in the vicinity of single grain boundary investigated through nanoindentation technique

Takahito Ohmura · Kaneaki Tsuzaki

Abstract The initiation of plasticity and the subsequent state in the vicinity of a single grain boundary during indentation-induced deformation were investigated to understand an elementary step of a stress-strain behavior of polycrystalline materials. Nanoindentation measurements on several points on a single grain boundary and the grain interior of an interstitial-free steel and an analysis on the pop-in behavior and the plastic nanohardness were carried out. The pop-in load P^c that was obtained on the loading curve is different for each measurement. However, the loading curves overlap one another and the unloading curves coincide as well after the pop-in event. The nanohardness Hn has no dependence on the P^c in the range of 150–550 μN. The relation between P^c and Δh can be expressed as a simple cubic polynomial function based on a geometrically necessary dislocation loop model. The fitted function differed for various grains with different crystallographic orientations.

Introduction

The grain boundary effect is one of the most important factors dominating the mechanical properties of ultra-fine grain materials. Classic models such as the dislocation pile-up model [1, 2], the dislocation source model [3] and the geometrically necessary dislocation model [4] have been used to explain the grain boundary efficiency. However, experimental works are still important and necessary to understand the total mechanism of grain-refinement strengthening. Previous studies on the mechanical characterization regarding this issue were only conducted in a macroscopic scale and could not separate the grain boundary effect from other strengthening factors because of the limitations in the experimental technique. One of the best approaches for understanding the grain boundary effect is to reveal an interaction between a single grain boundary and dislocations. The experimental method is confined to transmission electron microscopy observation [5–9] because the corresponding scale in sub-micron is rather small with this method. The nanoindentation technique makes it possible to probe the mechanical properties in nano-scale. A previous study [10] in niobium using the nanoindentation technique showed a strain burst during indentation called the ''pop-in'' phenomenon when a plastic zone crossed a grain boundary, suggesting that a single grain boundary has significant resistance to slip transfer. Another work [11] in martensitic steel demonstrated visually that grain boundaries have some resistance to dislocation glide motion even for a low-angle grain boundary through nanoindentation with a transmission electron microscope. The present authors made a nanoindentation measurement for steel and found that the pop-in phenomenon occurs at a low stress in the vicinity of the grain boundary [12]. The details of the deformation behavior must be investigated quantitatively for a better understanding of the single grain boundary efficiency. In this study, the nanoindentation-induced deformation behavior is investigated for a single grain boundary and the grain interior to understand the

T. Ohmura (✉) · K. Tsuzaki
Structural Metals Center, National Institute for Materials Science, Tsukuba, Ibaraki 305-0047, Japan
e-mail: ohmura.takahito@nims.go.jp

relationship between the pop-in phenomenon on the loading curve and the nanohardness calculated from the unloading curve as an initiation of plasticity and the subsequent state of deformation, respectively.

Experimental

A Ti-added ultra-low carbon interstitial-free steel (hereafter called IF steel) was used in this study. The chemical composition of the steel is shown in Table 1. An ingot was hot-rolled at temperatures from 1200 to 940 °C and cooled in a furnace. The typical grain size of this sample is about a couple hundred μm. All the specimen surfaces for nanoindentation testing were mechanically polished, and subsequently electropolished in a solution of 8% perchloric, 10% butylcellosolve, 60% ethanol, and 22% water at 0 °C under a potential of 40 volts to remove the damaged layer. Nanoindentation experiments were carried out using a Hysitron, Inc. Triboindenter. A Berkovich indenter was employed, and the tip truncation was calibrated using a reference specimen of fused silica. Analyses for the tip calibration and the calculation of hardness were conducted using the Oliver and Pharr method [13]. Probed sites and indent configurations on the specimen surfaces were confirmed before and after the indentation measurements with the scanning probe microscope (SPM) capabilities of a Triboindenter.

Results and discussion

Figure 1a shows a SPM image of the sample surface including a grain boundary. The grain boundary that appears from the upper left to the lower right is indicated by arrows. A triangular shaped indent mark can be seen exactly on the grain boundary. According to an analysis by electron back-scatter diffraction [12], the grain boundary has a misorientation of 30 ± 0.5° with a rotation axis of [3, 3, 28], and is a random boundary. An etching rate during electropolishing depends on a crystallographic orientation so that there is a step at a grain boundary leading to a visible grain boundary with SPM. However, the step at a grain boundary may cause an error when an indentation is made on the grain boundary. To make sure a
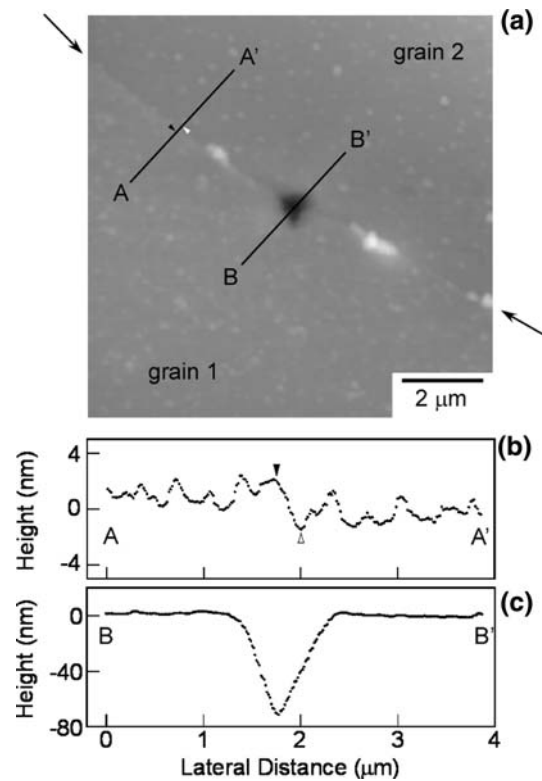

Fig. 1 Scanning probe microscope image of the specimen surface of the interstitial-free steel after indentation measurements. (**a**) the indent mark is made on the grain boundary, (**b**) and (**c**) the cross section profile along lines A–A′ and B–B′ which are indicated on the top view image of (**a**)

geometrical condition at the grain boundary, cross-section profiles of the sample surface along the lines A–A′ and B–B′ drawn on Fig. 1a are represented in Fig. 1b, c, respectively. Note that the height in the y-axis is enormously magnified compared to the lateral direction especially in Fig. 1b. The profile of the surface of the grain interior on grains 1 and 2 shown in Fig. 1b is very flat with a RMS roughness of 1.2 nm. The solid and open triangles on the profile represent the location of the head and the bottom of the "cliff" at the grain boundary corresponding to those on line A–A′ in Fig. 1a. The vertical distance (height difference) between the triangles at the grain boundary is 3.5 nm, which is very small and is the same with the peak-to-peak height in the grain interior. Figure 1c shows a surface profile that includes an indent mark after indentation. The depth of the indent mark is

Table 1 Chemical composition of the Ti added ultra-low carbon interstitial free steel (mass%)

C	Si	Mn	P	S	Al	Ti	N	O	B	Fe
0.0017	0.022	0.147	0.001	0.0002	0.028	0.051	0.0016	0.0014	0.0002	Bal

about 70 nm, which is much larger than the height difference at the grain boundary and the surface roughness on the grain interior. Therefore, an error in nanoindentation measurements could be vary small and negligible in the present condition. Figure 2 shows typical load-displacement curves for (a) the grain interior and (b) on the grain boundary. An obvious pop-in behavior is visible on both loading curves, and a critical load P^c and an excursion depth Δh can be defined as shown in the figure.
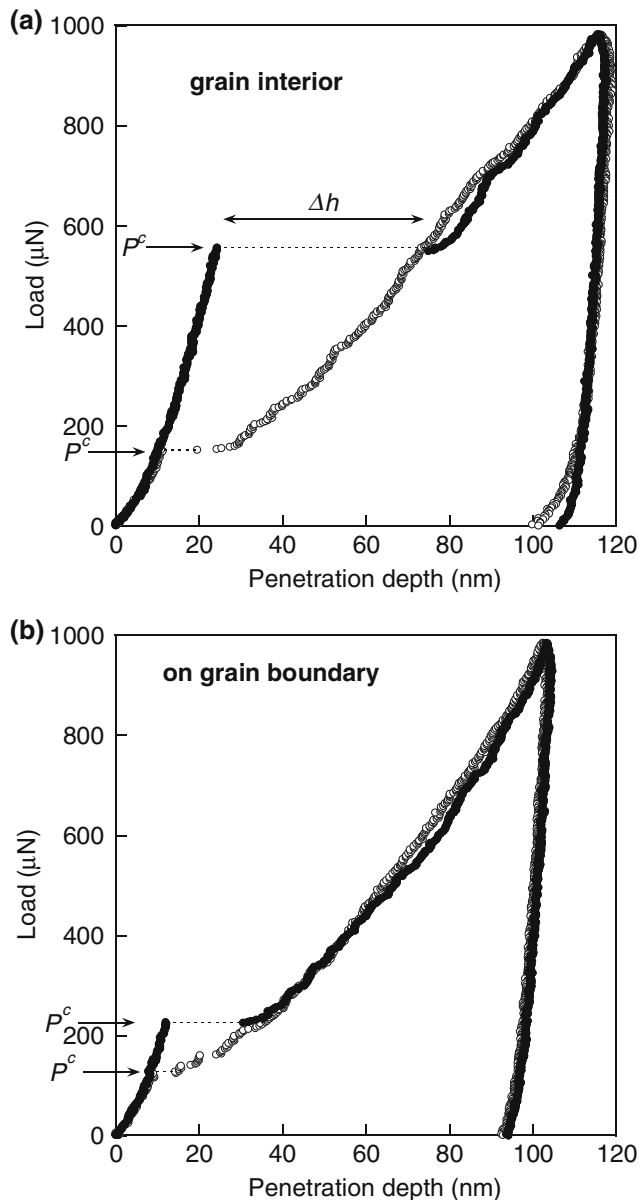

Fig. 2 Typical load-displacement curves for (**a**) "the grain interior" and (**b**) "on the grain boundary". Both curves have the obvious pop-in behavior. The critical load P^c and the corresponding excursion depth Δh are defined on the figure

Based on the Hertz contact theory [14], the pop-in phenomenon corresponds to the initiation of plastic deformation by drastic dislocation nucleation and/or multiplication [12]. The reason for the interpretation is as follows. The relation between a load P and a penetration depth h is expressed as

$$P = \frac{4}{3} E^* R_i^{\frac{1}{2}} h^{\frac{3}{2}}, \tag{1}$$

where R_i is a curvature of an indenter and E^* is the reduced modulus in the equation

$$\frac{1}{E^*} = \frac{\left(1 - v_s^2\right)}{E_s} + \frac{\left(1 - v_i^2\right)}{E_i}, \tag{2}$$

where E_s and v_s are the Young's modulus and the Poisson's ratio for the specimen, and E_i and v_i are the same parameters for the indenter. The loading curves below the pop-in load P^c are well fitted to Eq. (1), meaning that the deformation mode below the pop-in is purely elastic. Additionally, the maximum shear stress $\tau_{\max}$ underneath the indenter is given as [14]

$$\tau_{\max} = 0.18 \left(\frac{E^*}{R_i}\right)^{\frac{2}{3}} P^{\frac{1}{3}}. \tag{3}$$

Substituting the values of $E^* = 210$ GPa, $R_i = 230$ nm, and $P = 300$ μN as an average P^c for "the grain interior", the critical shear stress $\tau^c_{\max}$ is calculated to be 11.3 GPa. Since the shear modulus μ of ferrite is approximately 83 GPa, a ratio of $\mu/\tau^c_{\max}$ of 7.3 is obtained, which means that $\tau^c_{\max}$ is an order of an ideal strength of the ferrite phase. This suggests that the pop-in behavior is a plasticity initiation within a defect-free region.

The P-h curves in Fig. 2 also reveal some other interesting aspects of the deformation behavior. The pop-in load P^c is different for each measurement, and the difference is particularly large in "the grain interior". On the other hand, the loading and unloading curves overlap one another after the pop-in event. This indicates that the deformation behavior after the pop-in event does not depend on the plasticity initiation. This tendency is clear in the plots of the nanohardness Hn versus the pop-in load P^c for "on the grain boundary" and "the grain interior" in Fig. 3. The nanohardness Hn has no dependence on the P^c in the range of 150–550 μN, which corresponds to the range of $\tau^c_{\max}$ from 9.0 to 13.9 GPa from Eq. (3). The average nanohardness is higher for "on the grain boundary" than that of "the grain interior" while the average P^c is lower for "on the grain boundary". These results suggest that a
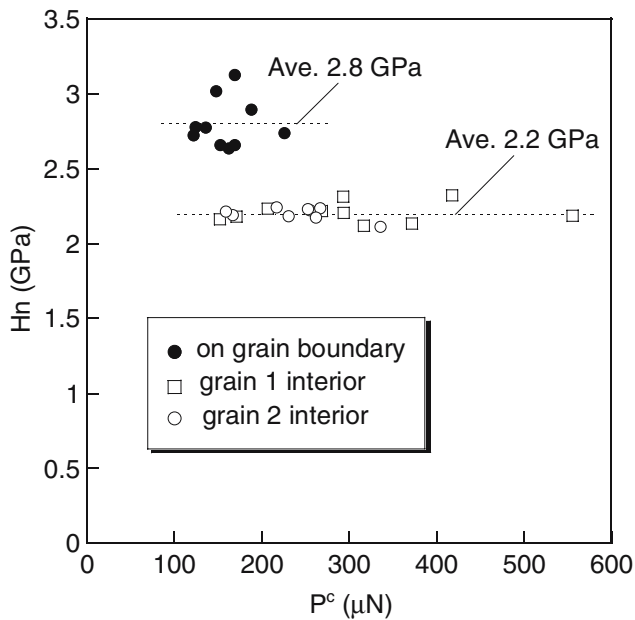
Fig. 3 Nanohardness Hn obtained from an analysis of the unloading curve versus the critical load P^c at the pop-in behavior on loading curves for "the grain interior" and "on the grain boundary" of the interstitial-free steel

Fig. 4 Relationship between the excursion depth Δh and the pop-in load P^c for "the grain interior" and "on the grain boundary" of the interstitial-free steel

subsequent state of plastic deformation after the pop-in event does not have any relation to the prior local plasticity initiation. The deviation in the P^c or τ^c_{max} could originate from a combination of factors such as a different critical shear stress to activate each dislocation source and a different applied shear stress at a source based on a distribution of a stress field beneath the indenter. Figure 2 shows that each curve has just one pop-in event and no other visible events on the subsequent loading curve. This suggests that once a dislocation source is activated, the dislocation density increases drastically and the other sources are generated by the dislocation interaction leading to a continuous plastic deformation, and the dislocation interaction dominates the plastic deformation in the subsequent state.

As shown in Fig. 2, the parameters P^c and Δh at the pop-in are obtained from the P-h curves. Figure 4 shows the relationship between the pop-in load P^c and the corresponding excursion depth Δh for "on the grain boundary" and "the grain interior". The data of grains 1 and 2 in the grain interior are represented by different marks. The Δh obviously increases with increasing P^c especially in the grain interior. To understand the relation of the plot, a deformation mechanism of the pop-in phenomenon is considered based on the model shown by Shibutani [15]. As described above, the pop-in event corresponds to a transition in the
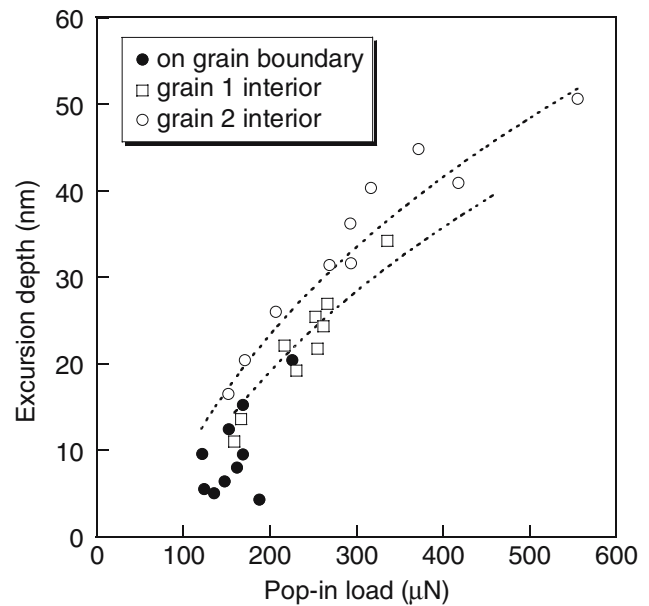
deformation mode from purely elastic to elastic-plastic. Therefore, the entire energy balance is

$$w^{total} = w^{plastic} + w^{elastic}, \tag{4}$$

where w^{total} is the elastic strain energy per unit volume before the pop-in, $w^{plastic}$ the plastic strain energy and $w^{elastic}$ the retained elastic strain energy per unit volume after the pop-in event. w^{total} is given as $w^{total} = \gamma^e \cdot \tau^c_{max}/2 = \tau^{c2}_{max}/2\,\mu$, where μ is a shear modulus. Using the geometrically necessary (GN) dislocation loop model [16], Δh is equal to nb, where n is a number of GN dislocations nucleated beneath the indenter, and b is a magnitude of Burgers vector as schematically shown in Fig. 5. When a contact radius is defined as a by assuming a conical indenter geometry in Fig. 5, the plastic strain γ^p is given as $\gamma^p = nb/a = \Delta h/a$. Therefore, $w^{plastic} = \tau^c_{max} \cdot \gamma^p = \tau^c_{max} \cdot \Delta h/a$. Substituting these parameters into Eq. (4), the τ^c_{max} is obtained as

$$\tau^c_{max} = \frac{2\mu}{a}\Delta h + \mu\gamma', \tag{5}$$

where γ' is the retained elastic strain after the pop-in. Combining Eqs. (3) and (5), the Δh is given as

$$\Delta h = 0.09\left(\frac{a}{\mu}\right)\left(\frac{E*}{R}\right)^{\frac{2}{3}}P^{c\frac{1}{3}} - \frac{a\gamma'}{2}. \tag{6}$$
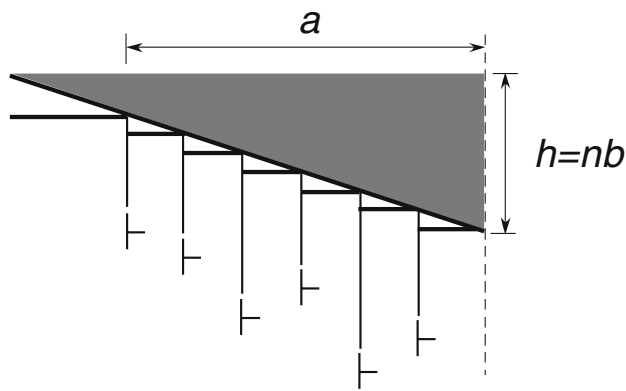
Fig. 5 A schematic drawing of geometrically necessary dislocations generated beneath an indenter. The Burgers vector is simplified to be parallel to the indentation axis that is perpendicular to the sample surface

Fitting the data of the grain interior in Fig. 4 to Eq. (6), the data of each grain roughly coincide with the broken lines of the simple cubic polynomial function. The fitted broken line of grain 1 is different from grain 2 as shown in Fig. 4. In other words, even if the P^c is the same, the corresponding Δh is not necessarily the same in all grains. This could be attributed to an effect of crystallographic orientation. In Fig. 5, the Burgers vector of the GN loop dislocation is assumed to be parallel to the indentation axis. However, actual dislocations could contain a Burgers vector with some deviation from the ideal geometry of Fig. 5. When we assume an angle θ between the Burgers vector and the indentation axis, Δh is given as $\Delta h = nb\cos\theta$. On the other hand, w^{plastic} is mainly composed of dislocation self energy and dislocation interaction energy. Since the both energy factors are an order of μb^2, w^{plastic} is almost proportional to $n\mu b^2$. If w^{plastic} depends on a crystallographic orientation, Δh should be different in each grain. If w^{plastic} with different crystallographic orientations is the same in various grains, then the number of dislocations generated at the pop-in event could also be the same. However, the values of Δh differ from each other by a different factor of $\cos\theta$ and may be one of the reasons for the different fitted broken lines of grains 1 and 2 in Fig. 4.

Summary

Indentation-induced plasticity initiation and subsequent deformation behavior were considered based on the analyses of pop-in behavior and nanohardness. Indentation measurements were made on different locations of "on the grain boundary" and "the grain interior" of interstitial-free steel, and the deformation behavior for the two cases were discussed. The pop-in load P^c obtained on the loading curve was different for each measurement. However, the loading and unloading curves overlapped one another after the pop-in event. The nanohardness Hn had no dependence on the P^c in the range of 150–550 μN. This indicated that the deformation behavior after the pop-in event did not depend on the local plasticity initiation. The relation between P^c and Δh was well fitted to a simple cubic polynomial function based on the geometrically necessary dislocation loop model. The fitted function differed for various grains with different crystallographic orientations, which could be attributed to an effect of an angle deviation between the Burgers vector and the indentation axis resulting from the crystallographic orientation.

References

1. Hall EO (1951) Proc R Soc B 64:747
2. Petch NJ (1953) J Iron Steel Inst 174:25
3. Li JCM (1963) Trans AIME 227:239
4. Ashby MF (1970) Phil Mag 21:399
5. Hauser JJ, Chalmers B (1961) Acta Matell 9:802
6. Carrington WE, McLean D (1965) Acta Matell 13:493
7. Shen Z, Wagoner RH, Clark WAT (1988) Acta Metall 36:3231
8. Kurzydlowski KJ, Varin RA, Zielinski W (1984) Acta Metall 32:71
9. Lee TC, Robertson IM, Birnbaum HK (1990) Met Trans 21A:2437
10. Wang MG, Ngan AHW (2004) J Mater Res 19:2478
11. Ohmura T, Minor AM, Stach EA, Morris JW Jr (2004) J Mater Res 19:3626
12. Ohmura T, Tsuzaki K, Yin F (2005) Mater Trans 46:2026
13. Oliver WC, Pharr GM (1992) J Mater Res 7:1564
14. Johnson KL (1985) Contact mechanics. Cambridge University Press, Cambridge, UK, pp. 84–106
15. Shibutani Y, Koyama A (2004) J Mater Res 19:183
16. Nix WD, Gao H (1998) J Mech Phys Solids 46:411